Local and Global Assessment of the Flow around the Japan Bulk Carrier with and without Energy Saving Devices at Model and Full Scale

Michel Visonneau, G.B. Deng, Emmanuel Guilmineau, P. Queutey, J. Wackers

31st Symposium on Naval Hydrodynamics
Monterey, California, 11-16 September 2016

Local and Global Assessment of the Flow around the Japan Bulk Carrier with and without Energy Saving Devices at Model and Full Scale

M. Visonneau, G.B. Deng, E. Guilmineau, P. Queutey & J. Wackers
(LHEEA, CNRS / Ecole Centrale de Nantes, France)

ABSTRACT

This paper presents a computational study of the flow around the Japan Bulk Carrier (JBC) with or without an Energy Saving Device (ESD) in front of the propeller. This study first conducted at model scale was performed in the framework of the Tokyo 2015 Workshop on Numerical Ship Hydrodynamics. Configurations with and without ESD, with and without propeller are compared and analysed. Conclusions about the efficiency of this specific ESD at model scale are drawn. A detailed analysis of the local flow for the configuration without duct is also conducted and recent results obtained by using hybrid LES turbulence closure are used to shed some light on the flow physics. Finally, this paper is complemented with an assessment of the efficiency of the same ESD at full scale which is provided to evaluate the influence of scale effects in this specific context.

INTRODUCTION

This paper presents a computational study of the flow around the Japan Bulk Carrier (JBC) with or without an Energy Saving Device (ESD) in front of the propeller. By comparing computations and experiments on configurations equipped or not of ESD, one would like to check if CFD is able to predict and explain the gain of propulsive efficiency observed in the measurements. This study was performed in the framework of the Tokyo 2015 Workshop on Numerical Ship Hydrodynamics. During the workshop, the analysis of the results of the participants indicated that the JBC hull, characterized by a relatively high block coefficient, had a stern flow field more difficult to compute with the usual RANS approaches. Questions about the relative role played by discretisation and modelling errors were raised but no conclusion was firmly established during the workshop. Moreover, the local flow analysis conducted in the main vortex core led to apparent contradictions and doubts about the measurements. All these points are revisited in this article in the light of new unsteady computations based on an hybrid LES approach. All the computations which are presented in this paper, are performed with the solver ISIS-CFD which is briefly described in the first section. Then, a careful grid sensitivity analysis is described in the second section. In the third and fourth sections, configurations with and without ESD, with and without propeller are compared with available experiments with the help of a global and local flow analysis. While all the computations described in these sections are performed at model scale, the last section examines the scale effect on the Energy Saving Device efficiency and draws some conclusions about the reliability of model scale experiments or computations to assess ESD efficiency at full scale.

ISIS-CFD AT A GLANCE

The solver ISIS-CFD, available as a part of the FINE^{TM}/Marine computing suite distributed by NUMECA Int., is an incompressible unsteady Reynolds-averaged Navier-Stokes (URANS) method mainly devoted to marine hydrodynamics. The method features several sophisticated turbulence models: apart from the classical two-equation k-ϵ and k-ω models, the anisotropic two-equation Explicit Algebraic Reynolds Stress Model (EARSM), as well as Reynolds Stress Transport Models, are available, see Deng et al. (1999) and Duvigneau & Visonneau (2003), with or without rotation corrections. All models are available with wall-function or low-Reynolds near wall formulations. Hybrid LES turbulence models based on Detached Eddy Simulation (DES-SST, IDDES) are also implemented and have been validated on automotive flows characterized by large separations (see Guilmineau et al., (2008)). Additionally, several cavitation models are available in the code. The solver is based on the finite volume method to build the spatial discretization of the transport equations. The unstructured discretization is face-based. While all unknown state variables are cell-centered, the systems of equations used in the implicit time stepping procedure are constructed face by face. Fluxes are computed in a loop over the faces and the contribution of each face is then added to the two cells next to the face. This technique poses no specific requirements on the topology of the cells. Therefore, the grids can be completely unstructured; cells with an arbitrary number of arbitrarily-shaped faces are accepted. Pressure-velocity coupling is enforced through a Rhie & Chow SIMPLE type method: at each time step, the velocity updates come from the momentum equations and the pressure is given by the mass conservation law, transformed into a pressure equation. In the case of turbulent flows, transport equations for the variables in the turbulence model are added to the discretization. Free-surface flow is simulated with a multi-phase flow approach: the water surface is captured with a conservation equation for the volume fraction of water, discretized with specific compressive discretization schemes, see Queutey & Visonneau (2007). The technique included for the six degrees of freedom simulation of ship motion is described by Leroyer & Visonneau (2005). Time-integration of Newton's law for the ship motion is combined with analytical weighted or elastic analogy grid deformation to adapt the fluid mesh to the moving ship. To enable relative motions of appendages, propellers or multiple bodies, sliding and overlapping grids approaches have been implemented. Propellers can be modeled using actuator disc theory, by coupling with boundary element codes (RANS BEM coupling, see Deng et al, (2013), or with direct discretization through the rotating frame method or sliding interface approaches. Finally, an anisotropic automatic grid refinement procedure has been developed which is controlled by various flow-related criteria, see Wackers et al. (2014). Parallelization is based on domain decomposition. The grid is divided into different partitions, which contain the cells. The interface faces on the boundaries between the partitions are shared between the partitions; information on these faces is exchanged with the MPI (Message Passing Interface) protocol. This method works with the sliding grid approach and the different subdomains can be distributed arbitrarily over the processors without any loss of generality. Moreover, the automatic grid refinement procedure is fully parallelized with a dynamic load balancing working transparently with or without sliding or overlapping grids.

THE JAPAN BULK CARRIER

The Japan Bulk Carrier (JBC) is a Capesize bulk carrier equipped with a stern duct as an energy saving device (ESD). National Maritime Research Institute (NMRI), Yokohama National University and Ship Building Research Center of Japan (SRC) were jointly involved in the design of this ship hull, duct and propeller. Its length between perpendiculars is L_{pp}=280m. Its service speed is 14.5 knots, leading to a Froude number Fn=0.142 and a Reynolds number at model scale of Re=7.46 10^6 with L_{pp}=7.00m at model scale. This ship was selected as one of the testcases of the Tokyo2015 workshop on numerical ship hydrodynamics, the latest edition in a series of workshops which also includes Gothenburg 2010 (Larsson et al., 2013). Towing tank experiments, including resistance tests, self-propulsion tests and PIV measurements of stern flow fields, were performed at NMRI, SRC and Osaka University. Several test cases were considered, all with free sinkage and trim; test cases C1 (resp. C2) are for towing test without (resp. with) ESD, cases C3 (resp. C4) for self-propulsion tests without (resp. with) ESD (see Table 1). Global force measurements and local LDV velocity profiles at three sections named S2, S4 and S7 (i.e. X/L_{pp}=0.9625, X/L_{pp}=0.9843 and X/L_{pp}=1.0000) before and after the propeller and duct were also provided by the organizers. Figs.1(a) and 1(b) show a view of the stern without and with ESD with the location of the local measurement sections.

(a) Without ESD

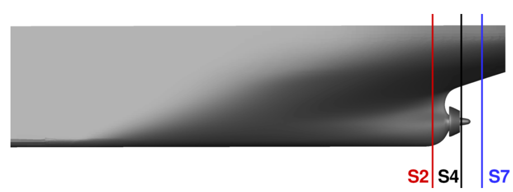

(b) With ESD

Figure 1: Side views of the JBC hull

Table 1: Definition of the test cases

Test case	C1	C2	C3	C4
Propeller (Self-propulsion)	No	No	Yes	Yes
Energy Saving Device	No	Yes	No	Yes

SOLUTION VERICATION PROCEDURE

Introduction

It is well accepted now that CFD (Computational Fluid Dynamics) is a mature tool for steady-state ship hydrodynamic applications such as resistance in calm water. Accurate enough predictions can be obtained with reasonable resources even for fully appended hulls, both for model and full scale in a routine design procedure. However, rigorous V&V (verification & validation) exercises are seldom performed by CFD users. In most of the cases, one grid and one computation are adopted following guidelines based on recommendations and experience. The recommended setup (such as grid density, turbulence model, etc.) may differ from one institution to another. Comparison with measurement data is often the only criterion when establishing those guidelines. The versatility of a guideline thus established can be questionable, since a small comparison error can be the result of error cancellation between numerical discretization and physical modeling errors. By performing a careful V&V exercise, one attempts to quantify turbulence modeling error and tries to answer questions such as whether a non-linear turbulence model is more accurate than a linear turbulence model for ship resistance prediction, what is the impact on the accuracy when a wall function is used, etc.

Compared with resistance computations, validation for propulsion computations is much more challenging. To our knowledge, the only approach capable of accurately predicting ship propulsion power is to simulate directly the rotating propeller with sliding grid or overset approaches. Time-accurate simulation with very small time steps is required for such simulation even if time-averaged solution is sufficient. Our experience with V&V exercises show that reliable numerical uncertainty estimations are nearly impossible in self-propulsion due to the high iterative error as well as the time discretization error, since the computations are performed without aiming at a time-accurate solution. Self-propulsion simulations may rely on a model representing the effect of the propeller by body forces in the RANS solver. With such an approach, propeller thrust can be provided by the RANS solver. But to determine propeller revolution rate and propeller torque, a simplified model or a coupling approach between RANS solver and another specific solver simulating the propeller such as RANS/BEM coupling approach must be used. The use of different numerical solvers to determine the self-propulsion point, makes a rigorous verification study almost impossible. This explains why the verification study described in the next sections will only concern the resistance computations.

General information

Except for the case when propeller motion is resolved by the RANS solver, only a half domain is simulated. For model and full scale simulations, the inlet boundary is located at 2.5L_{pp} from FP (forward perpendicular), the outlet at 3.0L_{pp} after AP (aft perpendicular). Bottom and top boundaries are located at 1.5L_{pp} and 0.5L_{pp} from the waterline, respectively. The lateral boundary is located at 1.5L_{pp} from the mid plane. A pressure boundary condition is applied at the bottom and top boundaries, while a far-field boundary condition is used at the inlet, outlet, as well as the lateral boundary.

Grid verification study

It is well known that it is perilous to use Richardson extrapolation to conduct a solution verification exercise when the computations are performed on fully unstructured grids. Actually, the Richardson extrapolation can be applied only when grid similarity is ensured. With the unstructured hexahedral mesh generator HEXPRESS™available in FINE™/Marine and employed in the present study, it is hardly possible to generate a set of rigorously similar grids. However, with a special setup, it is possible to ensure grid similarity before the insertion of viscous layer. This section does not aim at presenting the meshing algorithm and technology behind HEXPRESS™but to explain how similar grids can be built using this powerful software.

After importing the body geometry and defining the bounding box of the computational domain, a first mesh, namely medium mesh, is defined from an initial Cartesian subdivision with multiples of 4 and a refinement diffusion of 3. From that medium mesh, coarser or finer meshes can be generated, respectively, by decreasing or increasing the Cartesian subdivisions in one fourth of the initial values and decreasing or increasing in one unit the refinement diffusion parameter r_D. In case of using a low Reynolds number model for the wall modelling approach, the y^+ value of each mesh is adjusted proportionally to the initial element size for each new grid. However, for the wall-function modelling approach the viscous insertion parameters are kept unchanged. An example of this procedure for the definition of four similar grids geometrically embedded is given in Tab. 2 and illustrated in Fig. 2 before inserting the viscous layer.

It can be noticed in Tab. 2 that following this procedure the refinement ratio along the grid series is not constant, and its value decreases as more finer meshes are generated. These grids are geometrically embedded and grid similarity is fulfilled as long as the viscous layer is not inserted (Fig. 2). After the viscous layer insertion,

Table 2: Definition of similar grids

Mesh	Subdivision			y^+	r_D
	X	Y	Z		
Medium-Fine	10	10	10	0.80	4
Medium	8	8	8	1.00	3
Medium-Coarse	6	6	6	1.33	2
Coarse	4	4	4	2.00	1

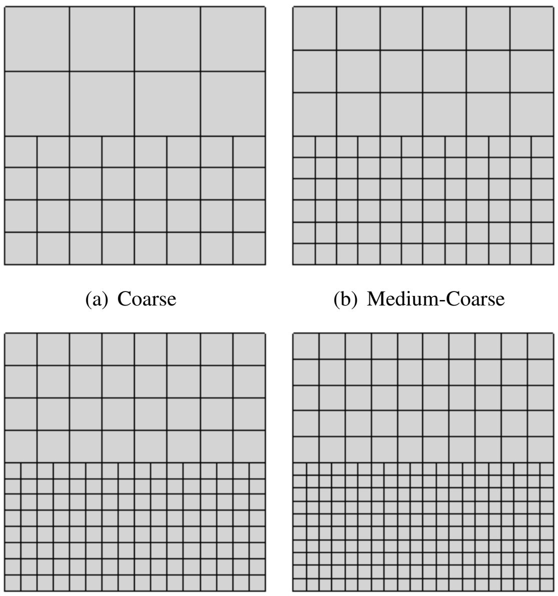

(a) Coarse (b) Medium-Coarse (c) Medium (d) Medium-Fine

Figure 2: Example of similar grids before inserting the viscous layer

part of the grid similarity is lost, penalizing the observed order of accuracy computed in the solution verification.

In order to ensure grid similarity as much as possible when the viscous layer is inserted, two different actions are done depending on the wall approach:

- Wall-function: y^+ is set to 30 and the number of sub-layers inside the viscous layer is adjusted for each grid.
- Near-wall: the number of sub-layers inside the viscous layer is kept constant between grids, but y^+ is equal to 0.16 for grid 1, 0.20 for grid 2, 0.27 for grid 3 and 0.40 for grid 4.

Our experience shows that grids thus generated usually allow a successful Richardson extrapolation. A series of four similar unstructured grids are generated, which are presented in Table 3.

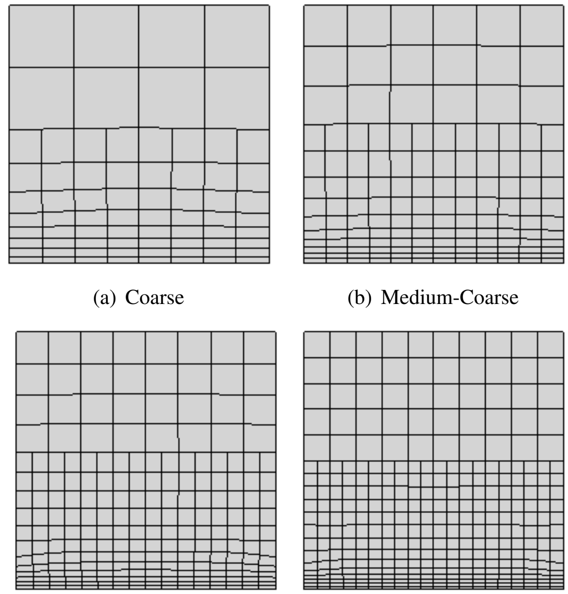

(a) Coarse (b) Medium-Coarse (c) Medium (d) Medium-Fine

Figure 3: Example of similar grids after inserting the viscous layer

Table 3: Number of grid cells for different cases

Cases	Grid 4	Grid 3	Grid 2	Grid 1
C1 $_{wm}$	405K	1.512M	3.143M	5.724M
C1 $_{wr}$	861K	2.632M	5.304M	9.197M
C2 $_{wm}$	725K	2.311M	4.806M	8.750M
C2 $_{wr}$	1.317M	4.269M	8.344M	14.077M
C3 $_{wm}$	2.442M	4.784M	10.247M	18.676M
C4 $_{wm}$	2.513M	6.668M	13.913M	25.332M

In Table 3, "wm" stands for wall modelled simulation for which wall function approach is used, "wr" for wall resolved simulation for which a near wall low-Reynolds turbulence model is employed. For the first case, the same y+ value of about 30 is applied for all grids, while for the second case, the y+ value changes from about 0.4 for the coarsest grid to about 0.16 for the finest grid. Meshes for different configurations have similar grid density. The difference in number of cells is due to the presence of the energy saving device (ESD) and the propeller, additional cells in the viscous layer when using wall resolved approach, and whole domain simulation rather than half domain simulation. Mesh density is not too fine since the mesh size near the free-surface is about $0.0008L_{pp}$ for the fine mesh. Grids 1 and 2 illustrate meshes commonly used for resistance computation for engineering application. Unless otherwise stated, all computations were performed with the non-linear EARSM turbulence model. A second-order upwind blended scheme was employed for spatial discretization except for the case with propeller resolved simulation for which a more stable AVLSMART scheme is used, see Pržulj & Basara, (2001).

ANALYSIS OF THE MODEL SCALE FLOW

Resistance results

Tables 4 and 5 give main results for total resistance for case C1 (without ESD) and C2 (with ESD), respectively. We give only the finest grid solution U1, the observed order of convergence p, Richardson extrapolation error RE% defined as $(\delta_{RE} - U1)/(\delta_{RE} * 100)$, and the comparison error E%D defined as $(D - S)/(D * 100)$ where D is the measurement data. S=U1 is the simulation result and δ_{RE} is the result of the Richardson extrapolation. The least squared approach proposed by Hoekstra and Eca (2008) is used for Richardson extrapolation. When the observed order of convergence is higher than 2.1, Richardson extrapolation is obtained with assumed second-order accuracy. For both cases, the EARSM model gives better prediction than the SST model. Moreover, the numerical discretization error is smaller than the difference due to turbulence model for the fine grid. Hence, when the grid is fine enough, the EARSM model should give better prediction for ship resistance for this test case. The reason for the better performance with the EARSM model is due to the existence of a relatively strong aft-body vortex for this geometry. When the aft-body vortex is not so strong, the SST model should also be capable to give an accurate prediction for ship resistance as well. Even with a fine grid containing more than 6M cells, numerical discretization error for resistance computation is still about 2% at least. Hence, when the grid is further refined, the EARSM model is expected to under-estimate the resistance by about 4% for the case without ESD, and 3% for the case with ESD. This is confirmed by computations with adaptive grid refinement which give a comparison error of 3.1% for the case without ESD, and 2.2% for the case with ESD. For both cases, the use of wall function does not deteriorate too much the predicted result. The predicted resistance differs only by 0.1% and 0.45% respectively, which is much smaller that the discretization error. This observation justifies the use of a wall function for engineering applications due to much lower computation cost. Flow separation is observed on the ESD as shown in Fig. 4. This might explain why the comparison error, the Richardson extrapolation error, and the observed order of convergence are higher for the case C2 when the wall function is used.

Table 4: Total resistance for case without duct and propeller (case C1)

Simulation	U1	p	RE%	E%D
earsm$_{wm}$	4.209	2.07	-2.3	1.87
earsm$_{wr}$	4.213	1.94	-2.0	1.77
sst$_{wr}$	4.087	1.59	-3.2	4.71

Table 5: Total resistance for case with duct and without propeller (case C2)

Simulation	U1	p	RE%	E%D
earsm$_{wm}$	4.200	2.93	-4.3	1.48
earsm$_{wr}$	4.219	2.06	-2.3	1.03
sst$_{wr}$	4.093	1.67	-3.2	3.99

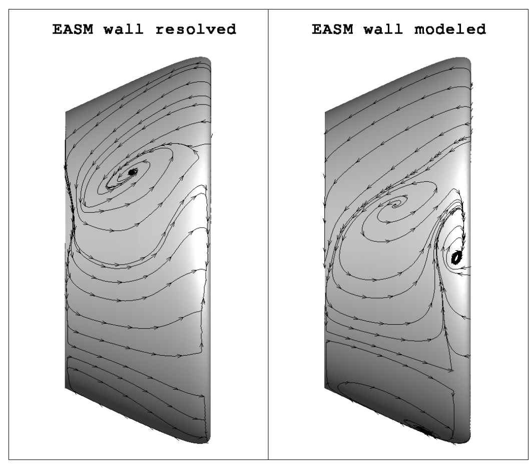

Figure 4: Wall streamlines on the duct for two wall modeling approaches

Predicting pressure resistance with good accuracy is a challenging task for CFD. Fig. 5 shows the Richardson extrapolation error for pressure resistance for the case without ESD. Even with the finest grid, the error is still about 10% for the EARSM model. Much higher uncertainty is observed for the SST model. But such high level of numerical uncertainty might be due to observed low order of convergence (1.53). Although pressure resistance represents only about 25% of the total resistance, the numerical error observed in total resistance comes mostly from pressure resistance error. For applications where the contribution of pressure resistance becomes more important, e.g. vessels with smaller L/B ratio, higher grid resolution might be needed to achieve acceptable accuracy.

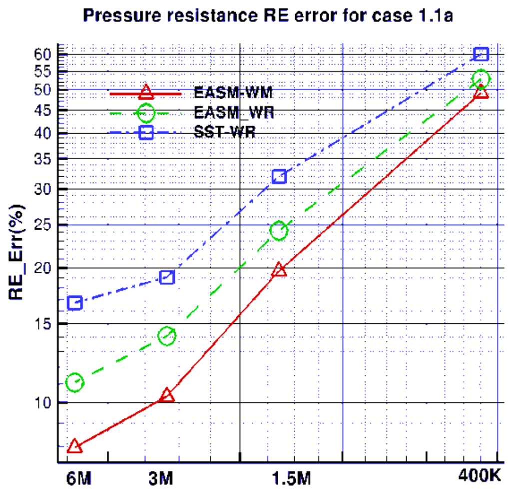

Figure 5: Richardson extrapolation for pressure resistance

Self-propulsion results

The most obvious approach to perform a self-propulsion computation is to simulate the rotating propeller with the RANS solver using sliding grid or overset grid approaches. A sliding grid methodology is employed in our computations. With such an approach, time-accurate simulation is required even when only time-averaged results are needed. A rigorous V&V study with such a procedure requires numerical uncertainty estimation on space and time. As explained before, due to high computational cost, it was not attempted to assess the time discretization error. Instead, the time step and the non-linear iteration number per time step were chosen according to open-water computations using the same grid for the propeller. Those parameters are chosen such that a sliding grid approach gives almost the same result for the propeller thrust compared with a computation performed in rotating frame. This "calibration" yields 150 time steps per revolution and 15 non-linear iterations per time step. One performs a first computation with a large time step to accelerate the ship to target speed until convergence. The rotating-frame approach is applied to the propeller domain. Ship trim and sinkage are computed during this computation. Then, in a restart computation, one switches to a small time step (150 time steps per revolution). Ship motion is frozen during this computation and therefore, during this restart, ship dynamic position is not computed exactly. In our propeller-resolved simulation, computations were performed with the EARSM model using wall function only. Computations were performed on 4 grids with different grid density as the cases for resistance computation. Figs. 6 and 7 show the evolution of force imbalance in our simulation for case C3 and C4, respectively. 0.5N imbalance represents about 1.2% ship resistance. The force imbalance is expected to vanish under self-propulsion condition. The raw data are highly fluctuating due to rotating propeller but results shown are smoothed by applying 1000 passes with the smoothing operation available in the Tecplot post-processor. The force imbalance obtained on the coarsest mesh is not shown but was very high (8N).

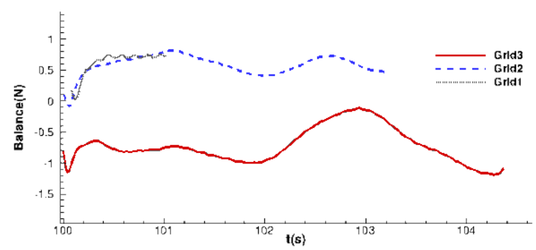

Figure 6: Force imbalance for case C3 (with propeller, without ESD)

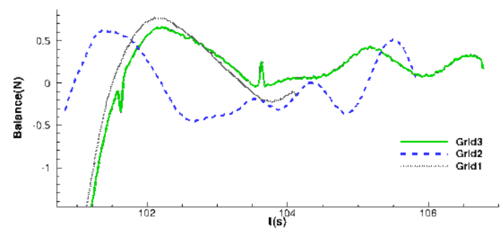

Figure 7: Force imbalance for case C4 (with propeller, with ESD)

Such high force imbalance is due to the very strong flow separation at the stern, resulting in a highly asymmetric wake. In our simulation, the propeller revolution rate was prescribed with the measurement value. Propeller thrust is positive. For the case without ESD, the force imbalance has a positive sign on the fine mesh (Grid1), i.e. propeller thrust is too high. One needs therefore to reduce propeller revolution rate to satisfy the self-propulsion condition. For the case with ESD, we are close to the self-propulsion condition. For case C4, we performed about 7 seconds of physical time, namely more than 50 propeller revolutions. With 150 time steps per revolution and 15 non-linear iterations per time step, the CPU cost is equivalent to about 30 resistance computations. Yet, it is hardly possible to determine a converged value for the force imbalance. Due to this convergence behaviour, we believe that the iterative error in our simulation is much higher than the discretization error. Hence, it is impossible to perform any reliable uncertainty estimation for a discretization error. Table 6 presents the predicted results with the finest grid for C_T, K_T and K_Q as well as relative errors compared with measurement data for cases C3 and C4. In spite of the high numerical uncertainty, the predicted results are in reasonable agreement with the measurements. High propeller torque is a typical result for RANS simulation when turbulence transition is not simulated. But as shown in the following section, the accuracy of the wake flow prediction can also be the cause of such an over-prediction as well. It should be stressed that propeller thrust and ship resistance are not clearly defined in a propeller-resolved RANS simulation. They are evaluated during post-processing using a procedure that is not always clearly defined. Concerning our results, it is considered that the dynamic axial force acting on the propeller domain is the propeller thrust. This choice is justified by the fact that the propeller thrust thus obtained agrees with the simulation using actuator disk approach presented later in this paper. With such a post-processing procedure, propeller thrust and ship resistance are under-estimated compared with measurement data. If one considers the axial force acting on propeller blades as propeller thrust, then for case C4, the propeller thrust and the ship resistance are under-estimated by 1.2% and 2%, respectively. This results in a better agreement with measurement data, while it is exactly the same simulation result. We have also performed self-propulsion simulations by using a body-force approach with an actuator disk model. Propeller thrust can be determined directly from the RANS computation. But to determine other quantities related to propeller performance, such as propeller torque and propeller revolution rate, a special coupling procedure is required. The RANS solver can be coupled with a BEM code or another type of simplified code to simulate the action of the propeller. In the present study, we employed a simpler approach without using any other simplified code. We only used the open-water K_T-K_Q results obtained from the measurements to determine the missing quantities in post-processing. The procedure is as follows. First, a usual RANS computation with an actuator disk approach is performed to simulate the effect of the propeller. Propeller thrust is adjusted during this computation such that a self-propulsion condition is satisfied. After having obtained the converged solution with the RANS solver, we compute the total velocity at the propeller plane. The total velocity is computed on a disk with the same size as the propeller diameter. This gives us two conditions: propeller thrust and total velocity. An additional open-water computation is performed using an actuator disk approach based on the open-water K_T-K_Q result. In this open-water actuator disk computation, propeller revolution rate and propeller advancing speed are adjusted such that the propeller thrust determined from the K_T-K_Q result and the total velocity computed at the propeller plane are the same as the values obtained with the RANS computation with the hull. With two conditions and two unknowns, the problem is well defined and can be solved iteratively. Compared with more complex coupling procedures such a RANS/BEM coupling approach, there is no need to compute the propeller induced velocity.

Table 6: Comparison error for propeller resolved simulation

	Case C3		Case C4	
	Value	E%D	Value	E%D
C_T*10^3	4.661	3.11	4.572	3.99
K_T	0.214	1.47	0.227	2.78
K_Q	0.029	-5.55	0.031	-3.52

Table 7: Propeller modeled simulation for case C3

	Wall resolved		Wall modeled	
	Value	E%D	Value	E%D
C_T*10^3	4.625	3.87	4.620	3.97
K_T	0.214	1.24	0.213	1.84
K_Q	0.0291	-4.41	0.0291	-4.19
n(rps)	7.60	2.56	7.62	2.31

Table 8: Propeller modeled simulation for case C4

	Wall resolved		Wall modeled	
	Value	E%D	Value	E%D
C_T*10^3	4.660	2.14	4.617	3.04
K_T	0.2385	-2.36	0.2327	0.13
K_Q	0.0306	-3.66	0.0305	-3.25
n(rps)	7.31	2.53	7.33	2.27

Unlike for resistance computations, it is hardly possible to obtain a result with a good convergence behavior with respect to the requirement for Richardson extrapolation. Therefore, only the predicted C_T, K_T, K_Q and propeller revolution rate n obtained with the finest grid as well as the relative errors compared with measurement data are shown in Tables 7 and 8 for the cases without and with ESD, respectively, both for wall resolved simulation and for wall modeled simulation using wall function. Unlike for propeller-resolved simulations, propeller thrust and ship resistance are clearly defined in the propeller-modeled RANSE computation. Compared with measurement data, predicted results are slightly better than what we obtained with the much more expensive propeller-resolved simulation presented in Table 6. As the computations are performed with half domain, propeller tangential forces are not taken into account. Errors due to this approximation need to be investigated in a future study. In our simulation, the measured K_T-K_Q are employed to determine propeller torque coefficient K_Q and propeller revolution rate n. Propeller torque is over-predicted in the propeller-resolved simulation. In spite of the uncertainty about the accuracy of such simplified approach, we believe that such overprediction of propeller thrust can be attributed to the accuracy of the predicted wake. As shown in the following sub-section, the predicted axial velocity at propeller plane is smaller than the measurement result, especially for the case without ESD. This explains why the estimated propeller revolution rate is lower and the propeller torque higher. In both cases, wall-resolved simulations and wall-modeled simulations give about the same accuracy. This justifies once again the use of wall functions for engineering applications.

Local Flow Results for JBC

Mesh influence on the flow around the naked hull without ESD nor propeller

The mesh set employed in the present study is designed to ensure an accurate enough accuracy for ship resistance and propulsion prediction based on our experiences. Spatial resolution in the wake near the propeller plane is about $0.00086L_{pp}$ with the finest grid. With such a grid resolution, the difference of the predicted axial velocity contours obtained with the two finest grids is still clearly visible as shown in Fig. 8, which means that a grid independent solution for the local flow field has not yet been reached. Therefore, computations with the adaptive grid refinement were performed tentatively to obtain a more accurate solution, first without taking into account the free-surface. Results obtained with a double model computation using wall resolved EARSM and adaptive grid refinement are shown in Fig. 9. The adaptive mesh contains about 35M cells located in regions of high shear but again, a significant difference can be observed between the computations and the measurements, indicating that the modeling error is likely to dominate the simulation despite the use of anisotropic EARSM turbulence closure.

In the core of the aft-body vortex, the predicted axial velocity is higher than measured, while for free-surface computations, the predicted value is lower. This indicates a non-negligible influence of the free-surface deformation on the flow field, despite the low Froude number Fn=0.142. To clarify this situation, we have performed another adaptive grid refinement computation with free-surface. The minimum cell size was refined to about $0.00009L_{pp}$. But with such a fine grid, a flow instability developed leading to an unsteady behavior of the large vortex structure. Due to this unexpected unsteadiness, the predicted wake flow becomes quite different from what is obtained when the numerical solution converged towards a steady solution. Such unsteadiness is also observed when the mesh is refined manually in the wake with similar grid resolution, although in that case, the amplitude of the unsteady fluctuation is not exactly the same. The flow around the naked JBC hull appears therefore to be difficult to be predicted accurately because

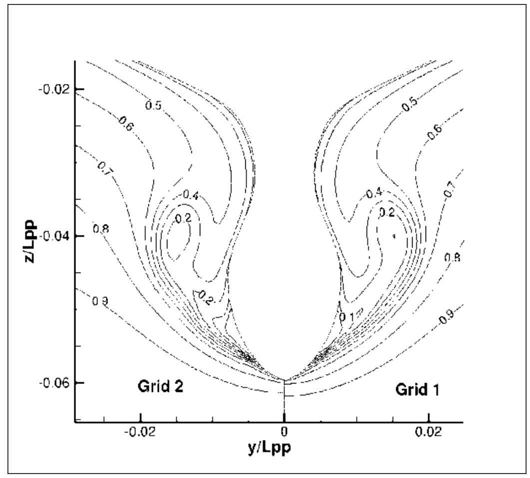

Figure 8: Case C1 - Predicted U velocity contours at section S2 - Grid influence

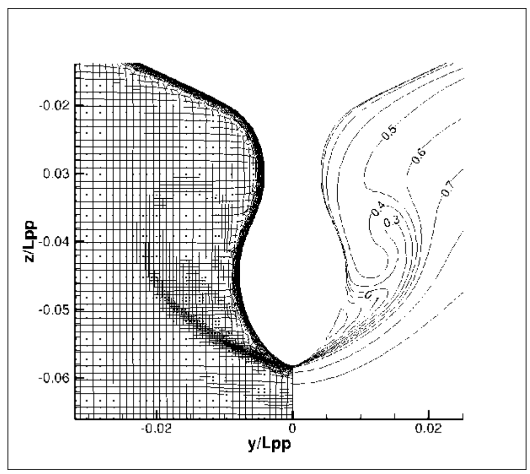

Figure 9: Case C1 - U velocity contours obtained with double model at section S2 with automatic grid refinement

of a likely unsteady behavior of the main vortex structure. Additional unsteady computations based on hybrid LES turbulence will be analysed later in this article in the section devoted to the local vortex core analysis in order to shed some light on this flow with complex physics.

Local flow comparisons with experiments without ESD nor propeller

Fig. 10 and 12 compare experiments with computed longitudinal velocity contours using the EARSM anisotropic turbulence model at sections S2 and S4. As pointed out previously, the computed longitudinal vorticity is slightly weaker than what is measured. As usually observed, the turbulence anisotropy present in the EARSM model contributes to a significant although insufficient increase of the longitudinal vorticity. Fig. 11 compares at section S2 the isotropic SST and the anisotropic EARSM turbulence closures.

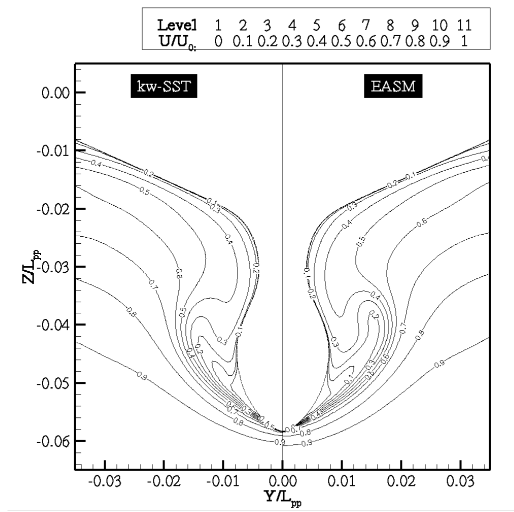

Figure 11: Case C1 - Comparison between SST and EARSM models at section S2

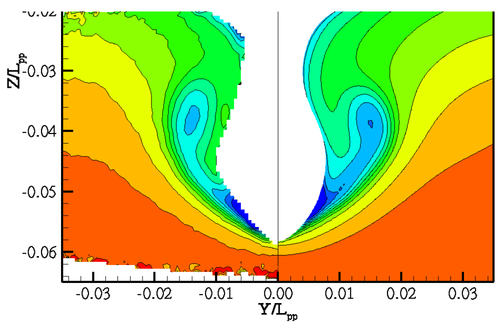

Figure 10: Case C1 - Comparison of U velocity contours at section S2 - Left: experiments, right: EARSM computations

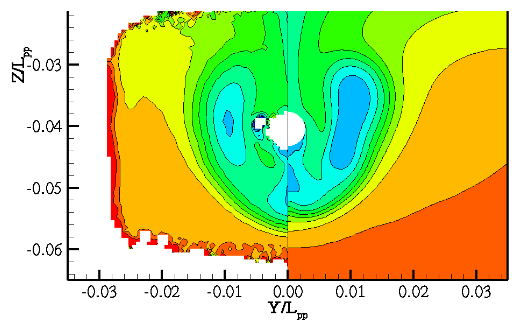

Figure 12: Case C1 - Comparison of U velocity contours at section S4 - Left: experiments, right: EARSM computations

Figs. 13 and 14 show the wall-resolved wall streamlines on the naked JBC hull without duct nor propeller. We can notice a slightly longer line of convergence indicating that the longitudinal bilge vortex is more pronounced with EARSM than with SST closures. Moreover, a relatively large zone of recirculation is visible at the stern below the propeller hub, which might be related with the unsteadiness noticed on very fine grids.

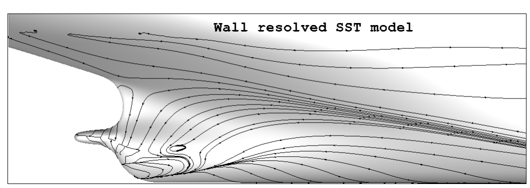

Figure 13: Case C1 - Wall streamlines with SST closure without duct

Local flow comparisons with experiments with ESD and without propeller

Figs. 15 and 16 show the wall streamlines around the hull with the presence of the duct for two different turbulence closures. The main effect of the duct is a suction effect which removes the spiral vortex which was detected by both turbulence closures just above the recirculation region located at the stern of the hull.

Figs. 17 and 18 show the experimental and computed isowake distributions at sections S2 and S4. We can observe that the presence of the duct increases the computed longitudinal vorticity, leading to an excellent visual agreement between the computations and the measurements at section S2. This agreement is confirmed at section S4 although the zone with negative longitudinal velocity seems to be slightly overestimated in the com-

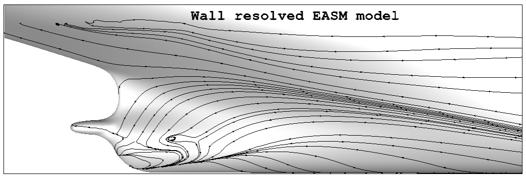

Figure 14: Case C1 - Wall streamlines with EARSM closure without duct

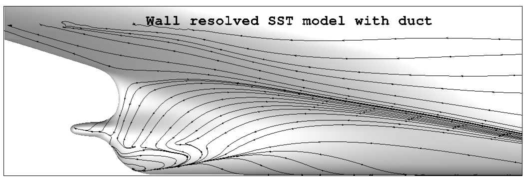

Figure 15: Case C2 - Wall streamlines with SST closure with duct

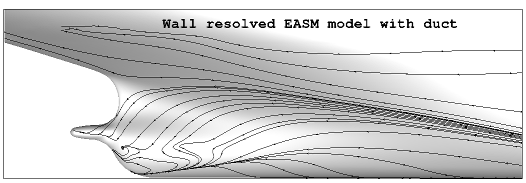

Figure 16: Case C2 - Wall streamlines with EARSM closure with duct

putations. This means that the local flow around the hull with a duct is easier to predict with a RANSE approach based on anisotropic turbulence closures than the configuration without duct, suggesting that the unsteadiness is reduced by the suction effect associated with the presence of the duct.

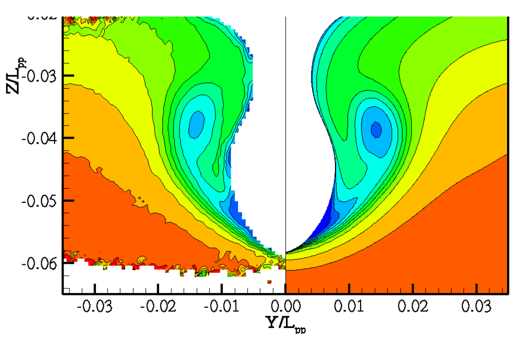

Figure 17: Case C2 - Comparison of U velocity contours at section S2 - Left: experiments, right: EARSM computations

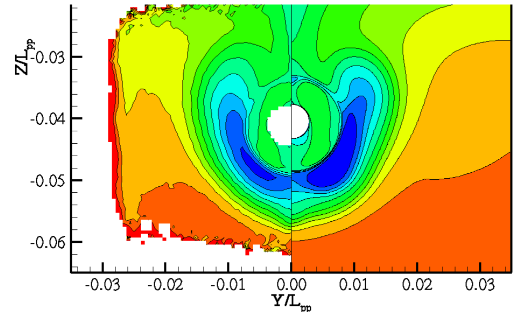

Figure 18: Case C2 - Comparison of U velocity contours at section S4 - Left: experiments, right: EARSM computations

Propulsive efficiency improvements due to ESD

Self-propulsion computations were performed both with or without ESD and two modeling approaches for the propulsion system, namely actuator disk (AD) and rotating propeller (RP) were used along this assessment. For the sake of conciseness, the local flow analysis will not be described in this article. Instead, one will focus this section on the influence of the Energy Saving Device on the global propulsion parameters. Figs. 19(a) and 19(b) show the duct propeller actual configurations.

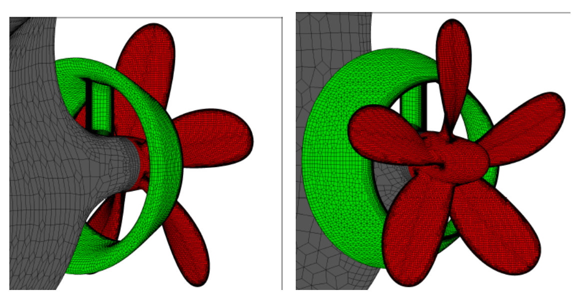

(a) Front view (b) Rear view

Figure 19: Views of the propeller + ESD

The following dimensionless coefficients are formulated:

$$K_T = \frac{T}{(\rho n^2 D^4)}; \quad K_Q = \frac{Q}{(\rho n^2 D^5)} \tag{1}$$

$$t = \frac{T + SFC - R_{T,Towing}}{T} \tag{2}$$

$$\eta_{OW} = \frac{J K_T}{2\pi K_{Q,OW}}; \quad \eta_R = \frac{K_{Q,OW}}{K_Q} \tag{3}$$

$$V_a = JnD \quad w_t = \frac{(U - V_a)}{U} \tag{4}$$

$$\eta_H = \frac{1-t}{1-w_t}; \quad \eta_D = \eta_{OW} \cdot \eta_R \cdot \eta_H \tag{5}$$

where T (resp. Q) is the thrust (resp. torque) of the propeller. SFC and $R_{T,Towing}$ stand for the Skin Friction Correction and the resistance in towing condition while $K_{Q,OW}$ is the torque coefficient in open water condition, n the number of revolutions per second and D the diameter of the propeller. J is the advance ratio, V_a the propeller advance speed and w_t the Taylor wake fraction. t, η_{OW}, η_R, η_H and η_D stand for the thrust deduction factor, propeller open water efficiency, relative rotative efficiency, hull efficiency and propeller quasi-propulsive coefficients, respectively. All these coefficients are summarized in Tab. 9 and Tab. 10 which allow us to compare the performance of each propulsion modelling approach in terms of efficiencies while using or not ESD. The coefficients for both Cases C3 and C4 have been computed using the simulations with the wall-function modelling approach.

Finally, both measurements and simulations have revealed an efficiency gain when the ESD is installed, confirming qualitatively the experimental observations. Nonetheless discrepancies appear between EFD and CFD on how much this gain is. The former has shown a gain in the propulsive efficiency of 6.5%, whereas the latter predicts a gain around $8.2\% - 9.0\%$ depending on the propulsion modelling approach.

LOCAL VORTEX FLOW ANALYSIS AT MODEL SCALE

Transversal vortex core analysis

In the previous sections, the local flow analysis was uniquely based on the inspection of the flow characteristics at specific cross-sections where experiments were available. Although this analysis is useful and necessary, it only provides a global picture of the flow for each experimental cross-section. In this section, a more detailed and local vortex flow analysis is presented in order to shed some light on the flow characteristics in the core of the vortex. This local analysis is performed on the free-surface flow around the JBC with no propeller and no ESD (experiments from NMRI, test case C1). Although several vortices were identified in the RANSE computations, for the sake of simplicity, the local vortex core analysis will be performed only on the main vortex shown in Fig. 20.

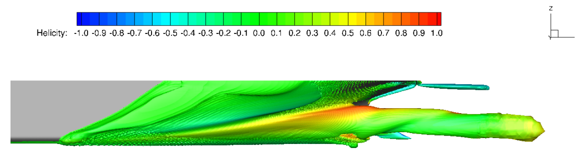

Figure 20: Side view of the vortical structures identified as iso-surfaces Q*=25

To define the main vortex center, one usually relies on the local maximum value of the invariant Q in order to keep a physical consistency. Without three-dimensional experiments, it is hardly possible to determine rigorously the experimental value of the invariant Q, and consequently, the local position of the experimental vortex. Therefore, it was decided to use the local maximum of the longitudinal vorticity as indicator of the experimental center of the vortex, which is satisfactory if the axis of the vortex is aligned with the x longitudinal direction. Comparisons between these two criteria computed from the computations indicated that the locations of the centers provided by these two criteria are very close for sections S4 and S7, which means that the local comparison with experiments are globally meaningful for these two sections and more questionnable at section S2. The transversal evolutions along horizontal and vertical lines across the vortex center are therefore computed at three specific cross-sections S2, S4 and S7. The horizontal and vertical ranges are determined within a range such that one stays inside the main averaged vortical structure. Figures 21 to 24 show these comparisons for the longitudinal component of the velocity (U) and the turbulent kinetic energy (TKE) for the above-mentioned sections. In these figures, Y_{v1} and Z_{v1} stand for the coordinates of the mean vortex center.

During the T2015 workshop, a satisfactory agreement was observed for the mean longitudinal component of the velocity in the core of the vortex while a very large difference between the experiments and computations for the turbulent kinetic energy (TKE) horizontal and vertical distributions was noticed. This trend was shared by all the participants using RANSE turbulence models, except Kornev's team who performed unsteady computations with an hybrid RANSE-LES turbulence model (Kornev at al., (2011), Abbas et al., (2015)). Although NMRI, which realized the experiments, was skeptical about the reliability of their TKE measurements, it was decided in Nantes to carry out such unsteady computations with a similar hybrid LES closure based on a DES-SST turbulence model already successfully used for automotive flows (see Guilmineau et al., (2008)) to

Table 9: Case C3 - Hull and propeller without duct - Summary of propulsive and efficiency coefficients

Parameter	EFD	AD		RP			
		Sim_1	$E\%D$	Sim_2	$E\%D$	Sim_3	$E\%D$
K_T x 10	2.170	2.130	1.84	2.154	0.74	2.144	1.20
K_Q x 10^2	2.790	2.907	-4.19	2.968	-6.38	2.977	-6.70
$K_{Q,OW}$ x 10^2	2.830	2.958	-4.51	2.835	-0.17	2.826	0.15
n	7.800	7.620	2.31	7.800	0.00	7.800	0.00
T	22.589	20.946	7.27	22.219	1.64	22.113	2.11
$R_{T,Towing}$	36.363	35.668	1.91	35.668	1.91	35.668	1.91
t	0.196	0.166	15.26	0.214	-9.13	0.210	-7.21
w_t	0.448	0.488	-8.92	0.432	3.60	0.429	4.32
J	0.411	0.390	5.06	0.423	-2.93	0.425	-3.51
η_0	0.5013	0.4470	10.83	0.5113	-2.00	0.5134	-2.42
η_R	1.0144	1.0175	-0.30	0.9552	5.84	0.9493	6.42
η_H	1.4575	1.6298	-11.82	1.3845	5.00	1.3833	5.09
η_D	0.7411	0.7412	-0.02	0.6762	8.77	0.6742	9.03

Table 10: Case C4 - Hull and propeller with duct - Summary of propulsive and efficiency coefficients

Parameter	EFD	AD		RP	
		Sim_1	$E\%D$	Sim_2	$E\%D$
K_T x 10	2.330	2.327	0.13	2.304	1.12
K_Q x 10^2	2.950	3.046	-3.25	3.097	-4.98
$K_{Q,OW}$ x 10^2	2.977	3.101	-4.18	2.871	3.53
n	7.500	7.330	2.27	7.500	0.00
T	22.435	21.214	5.44	21.966	2.09
$R_{T,Towing}$	36.288	35.752	1.48	35.752	1.48
t	0.189	0.168	11.30	0.196	-3.75
w_t	0.522	0.558	-7.02	0.502	3.86
J	0.370	0.350	5.51	0.386	-4.21
η_0	0.4615	0.4180	9.42	0.4929	-6.82
η_R	1.0090	1.0181	-0.90	0.9272	8.11
η_H	1.6949	1.8837	-11.14	1.6122	4.88
η_D	0.7892	0.8016	-1.58	0.7368	6.63

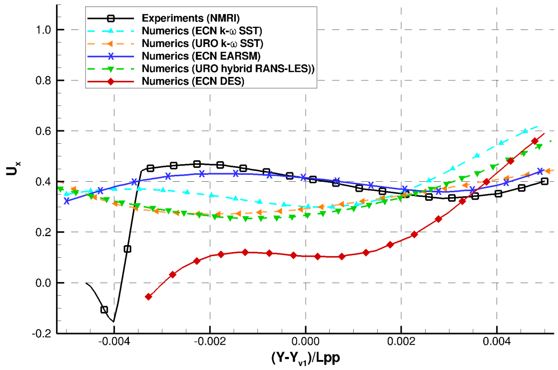

(a) Section S2

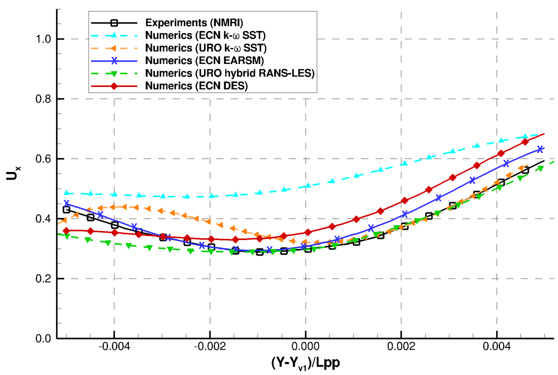

(b) Section S4

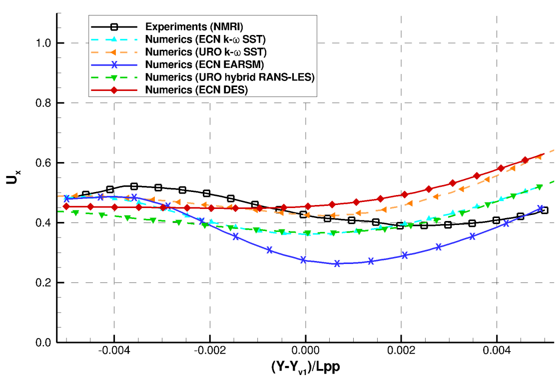

(c) Section S7

Figure 21: Case C1 - Horizontal evolution of U around the vortex center

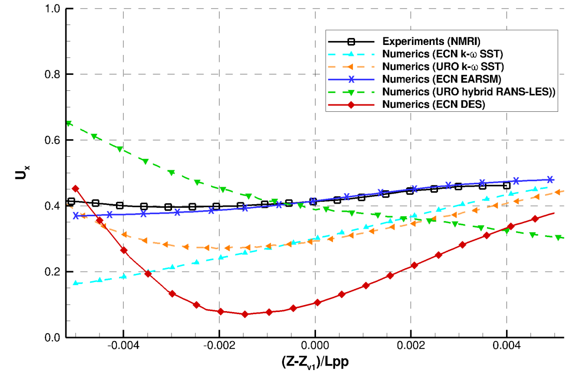

(a) Section S2

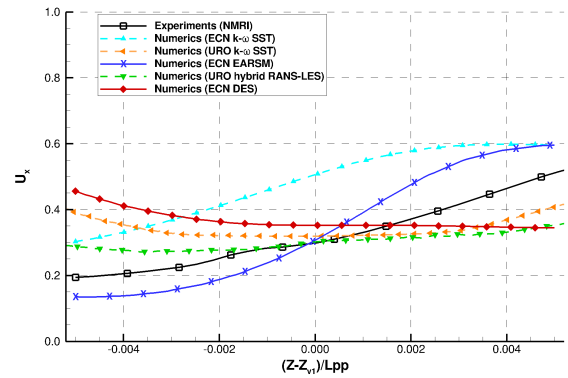

(b) Section S4

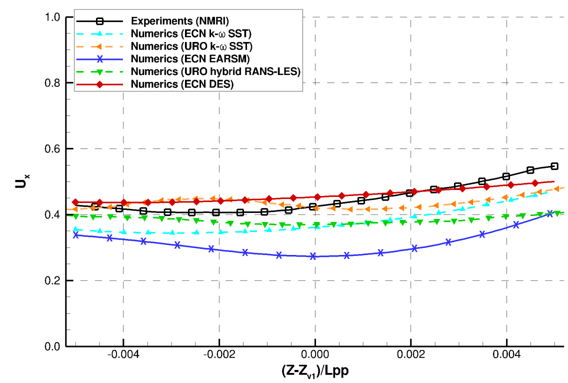

(c) Section S7

Figure 22: Case C1 - Vertical evolution of U around the vortex center

check if similar trends were observed independently of the solver. The new DES-SST computations were performed on a grid around the complete double-body hull comprised of 66 million points complying with the Taylor scale and a time step $\Delta t = 0.006s$. Figures 23 to 24 show such results for TKE and fully confirm the results obtained by Kornev et al. during the Tokyo2015 workshop.

The level of TKE computed with hybrid LES formulations, in very good agreement with NMRI measurements, is three to ten times higher than what is simulated by the isotropic or anisotropic RANSE models. The co-existence of high levels of TKE and large levels of longitudinal vorticity in the core of a vortex is somewhat contradictory in

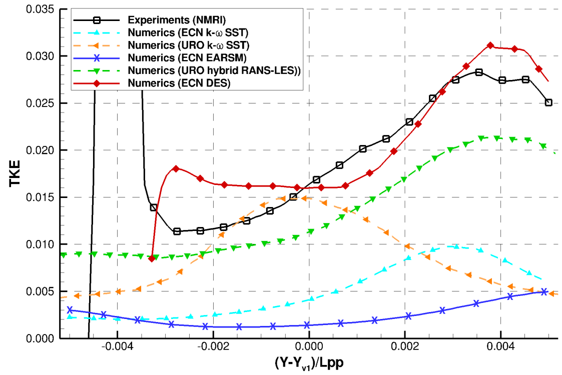

(a) Section S2

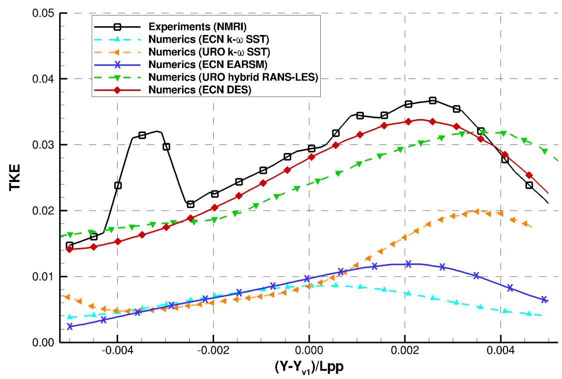

(b) Section S4

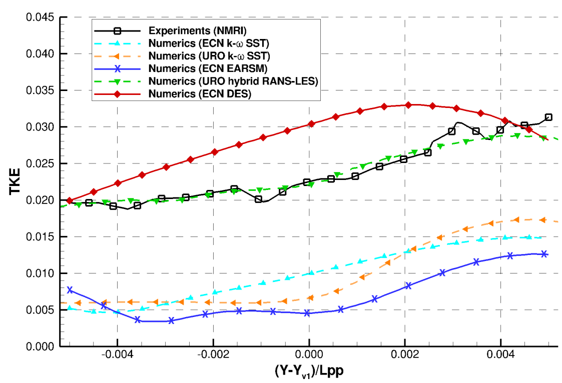

(c) Section S7

Figure 23: Case C1 - Horizontal evolution of TKE around the vortex center

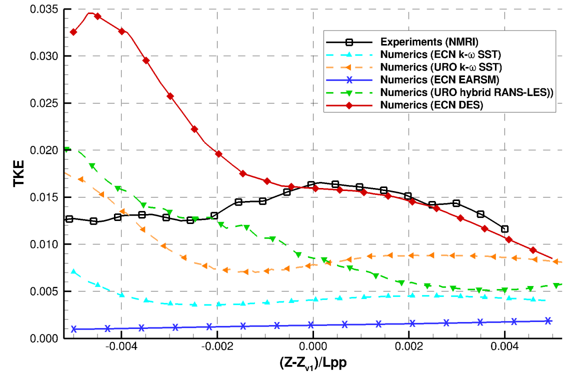

(a) Section S2

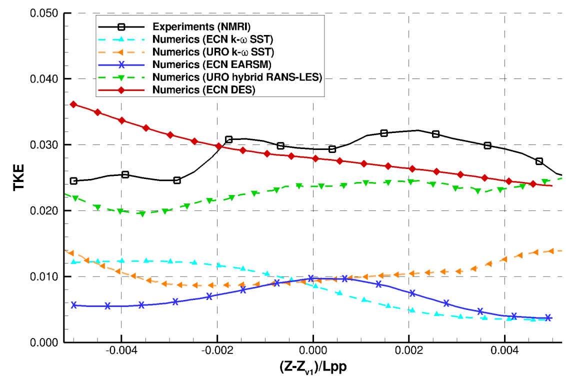

(b) Section S4

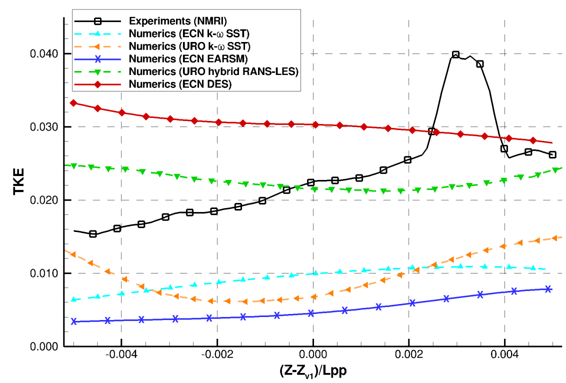

(c) Section S7

Figure 24: Case C1 - Vertical evolution of TKE around the vortex center

the framework of the RANSE paradigm, since high levels of TKE mean even higher levels of the turbulent viscosity, which contributes to the dissipation of the vortex and consequently reduces its vorticity. Such a chain of deduction is valid if we are in presence of a unique isolated vortex but, what was revealed by the unsteady DES-SST computations is that an isolated bilge vortex (at least for the JBC) is actually a kind of intellectual reconstruction which does not reflect the physical reality. In the case of the JBC, what is called an averaged bilge vortex is actually a superposition of intense and strongly unsteady smaller vortical structures. To support this interpretation, Fig. 25 provides two instantaneous views of the longitudinal vorticity at section S4 separated by ten time steps i.e. $0.06s$, extracted from the DES-SST computations.

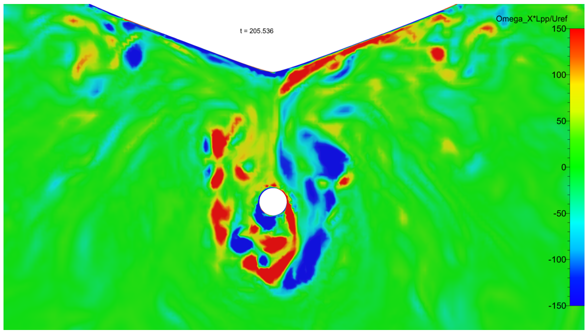

(a) Time 205.536s

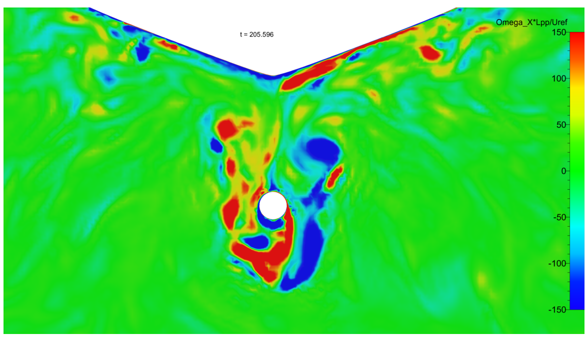

(b) Time 205.596s

Figure 25: Case C1 - Instantaneous views of the longitudinal vorticity at section S2

It is believed that this is the fundamental reason which can explain concomitant large levels of averaged turbulence kinetic energy and longitudinal vorticity. The unsteady motion of these smaller scale vortical structures contributes to a high level of TKE which is associated with relatively low frequency macroscopic fluctuations. This level of fluctuations is probably correctly measured by NMRI since the frequency of this evolution is clearly lower than the experimental measurement frequency (6Hz). Figure 26 showing a FFT decomposition of TKE at point (X=-3.391 m (i.e. 0.984428 L_{pp}), Y=-0.065949 m, Z=0.102806 m), exhibits two peaks at 0.833 Hz and 1.18 Hz, peaks which could have been captured by NMRI's experiments.

To understand the origins of this large scale unsteadiness, one should refer to Fig. 27 which gives an instantaneous view of the iso-surfaces of the Q invariant colored by the helicity. The figure clearly shows a succession of ring vortices which are created after the onset of an open separation linked with the initial thickening of the boundary layer illustrated by the convergence of the averaged wall streamlines (see Figure 28). This large scale unsteadiness is likely to be due to the peculiar design of

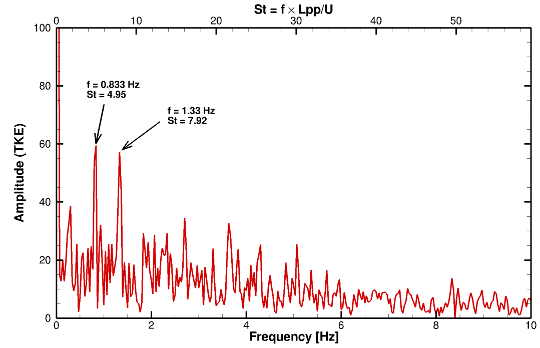

Figure 26: Case C1 - FFT decomposition of TKE

JBC (C_B=0.858). The rapid reduction of the hull sections at the stern, implied by the high value of C_B, creates the condition of open separation followed by a flow reversal and a strong unsteadiness revealed by the shedding of ring vortices. Figure 28 showing the averaged wall streamlines associated with the DES-SST computations, supports this analysis. This underlying physical unsteadiness may explain why the grid convergence on the local flow is difficult to reach with a RANSE approach and consequently, the mixed success of anisotropic EARSM turbulence closures. When the ESD is installed, the unsteadiness may be reduced due to the suction effect created upwind of this device, which explains the better agreement of RANSE computations for the local flow, as observed in figures 17 and 18. Finally, Fig. 29 shows the isowake distribution at section S4 computed with the above-mentioned DES-SST turbulence closure. Although the shape of the averaged isowake contours is very well represented up to $U = 0.4$, it appears that the contours $U = 0.3$ and $U = 0.2$ are missing, indicating that the local longitudinal flow in the core of the averaged vortex is still too strong. It is felt that this is due to the typical minimum cell sizes which are still too large to capture the smaller vortical separated flow structures which could contribute to the increase of the averaged longitudinal vorticity and associated reduction of the longitudinal velocity in the core of the averaged vortex. Additional computations on a finer grid with smaller time step are scheduled to assess this hypothesis.

FULL SCALE FLOW AROUND THE JBC

The previous sections were focused on the global and local studies of the model scale flow around the JBC with and without the presence of an energy saving device (ESD). The gain in terms of propulsive efficiency observed in the experiments was confirmed to some extent by the computations. To complete this study, it is interesting to assess the efficiency of the same Energy Saving

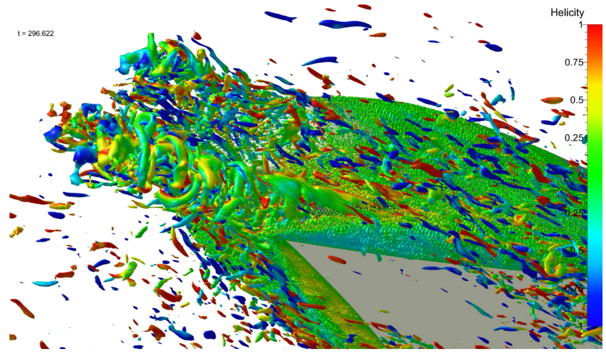

Figure 27: Case C1 - Instantaneous view of Q invariant colored by the helicity

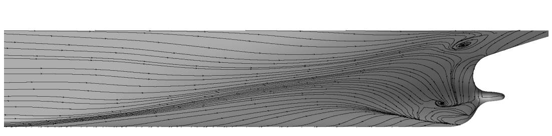

Figure 28: Case C1 - Wall streamlines with the DES-SST closure

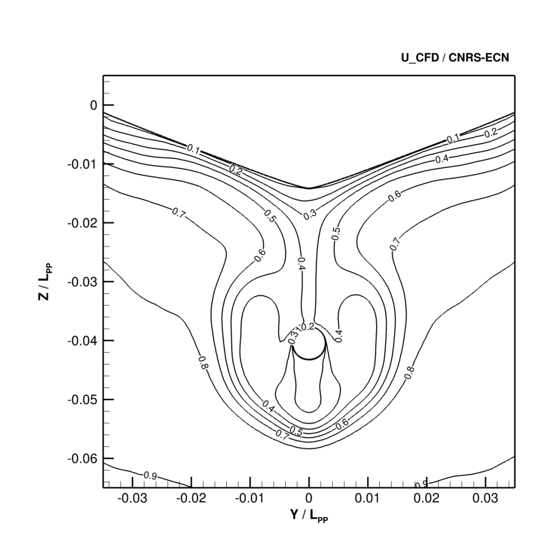

Figure 29: Case C1 - Isowake distribution at section S4 with DES-SST closure

Device at full scale in order to determine if one can use model scale experiments and computations to assess and optimize the design of such an ESD. Full scale computations were therefore carried out on grids comprised of 6.9M (resp. 10M) cells without (resp. with) ESD with a wall-function approach. For both computations, the free-surface was taken into account and the Reynolds number was $2.98\,10^8$.

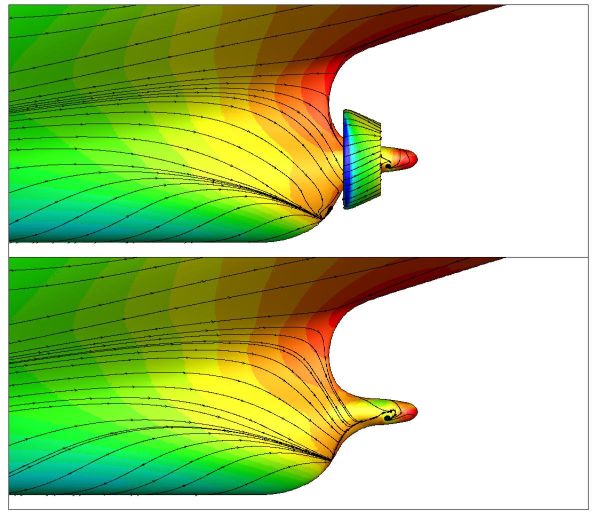

Figure 30: Wall streamlines at full scale with and without ESD

Fig. 30 shows the wall streamlines at full scale with and without duct. We can notice that the topology of the wall streamlines is completely different from what was computed at model scale. No more recirculation is visible at the stern part of the ship, which implies probably that the full scale turbulent flow is easier to compute and model with a RANSE approach.

Fig. 31 shows a comparison of the isowake distribution at model and full scale in front of the duct. At full scale, one can not see any large bilge vortex. It is therefore not surprising to find that the ESD is completely inefficient for the real ship as indicated by the propulsion coefficients computed in Table 11. It would be necessary to perform a systematic grid refinement study to provide a safer conclusion concerning the efficiency of this specific ESD at full scale. However, it is believed that the trends illustrated by this brief scale study establish that it is hopeless to design an ESD on the sole basis of model scale computations or experiments. In this case, the full scale delivered power with ESD exceeds the one without ESD by more than 10%, justifying the introduction of the new acronym EWD (Energy Wasting Device) to name it. Here again, having recourse to full scale computations and full scale shape optimization appears unavoidable.

CONCLUSION

This paper has presented a summary of computations performed on the Japan Bulk Carrier chosen for the last Tokyo 2015 workshop on numerical ship hydrodynamics. A grid influence study was carried out to evaluate the influence of the discretisation error on the resistance

Table 11: Propulsion coefficients at full scale without and with ESD

Parameter	Without ESD	With ESD
Ship speed U [m/s]	7.4566	7.4566
Towing resistance R_T [N]	1,075,600	1,104,700
Self propulsion resistance R_{Tsp} [N]	1,289,100	1,384,000
Propeller diameter D [m]	8.12	8.12
Density ρ [kg/m^3]	1,026	1,026
Propeller revolution rate n [rps]	1.2361	1.2166
Propeller torque Q [Nm]	1,394,254	1,457,626
Thrust coefficient K_T	0.18916	0.20964
Torque coefficient K_Q	0.02520	0.02719
Thrust deduction coef. $1-t$	0.83438	0.79819
Advance ratio J	0.48065	0.43207
Torque coefficient in open water $K_{Q,OW}$	0.025096	0.027068
Propeller advance speed V_a [m/s]	4.82423	4.26826
Taylor wake fraction w_t	0.35303	0.42759
Effective wake coefficient $1-w_t$	0.64697	0.57241
Open water efficiency η_{OW}	0.57660	0.53260
Relative rotative efficiency η_R	0.99604	0.99545
Propulsive efficiency η	0.74067	0.73930
Delivered power $P_d = 2\pi Qn$ [W]	10,828,413	11,142,089

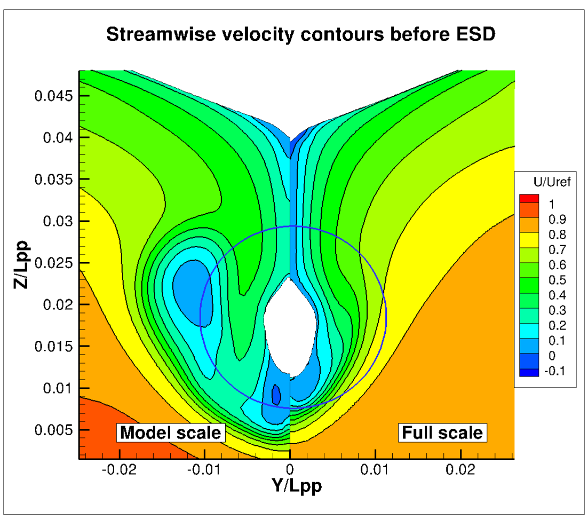

Figure 31: Scale effect on the isowake distribution in front of the ESD

and more specifically on the pressure resistance. Then, a comparison with available experiments was reported for the cases with and without ESD to try to quantify the influence of the duct on the local flow and consequently, on the propulsive efficiency. On the basis of the RANSE computations, the fine grid computations seemed to indicate that the flow was not fully steady everywhere. To gain a better understanding of the flow, unsteady hybrid LES computations were performed which showed a marked unsteady separation zone characterized by a wake of coherent ring-vortices periodically shed at the stern of the ship. These hybrid LES computations provided a new interpretation of the averaged stern flow which removed the contradiction between high levels of vorticity and turbulence kinetic energy in the core of the averaged vortex. Finally, an additional full-scale computation with the same ESD characteristics established that the propulsive efficiency of ESD is strongly affected by scale effects and underlined the need of designing ESD directly at full scale with the help of CFD.

ACKNOWLEDGMENTS

The computations were performed using HPC resources from GENCI (Grand Equipement National de Calcul Intensif) (Grant2015-2a1308, Grant2016-2a0129), which is gratefully acknowledged. Thanks are also due to Alvaro del Toro-Llorens who performed some of the computations reported in this article during his Master thesis.

REFERENCES

Abbas N., Kornev N., Shevchuk I. and Anschau P., "CFD prediction of unsteady forces on marine propellers caused by the wake nonuniformity and nonstationarity," Ocean Engineering Vol. 104, pp. 659–672, 2015.

Deng, G., and Visonneau, M., "Comparison of explicit algebraic stress models and second-order turbulence closures for steady flows around ships," Proc. 7th Int. Conf. on Numerical Ship Hydrodynamics, Nantes, France, 1999.

Deng, G., Queutey, P., Visonneau, M., and Salvatore, F., "Ship propulsion prediction with a coupled RANSE-BEM approach.," Proceedings of the V International Conference on Computational Methods in Marine Engineering, MARINE-2013, Hamburg, Germany, May 2013.

Duvigneau, R., and Visonneau, M., "On the role played by turbulence closures in hull shape optimization at model and full scale," J. Mar. Sci. Technol., Vol. 8, 2003, pp. 11–25.

Guilmineau, E., Chikhaoui, O., Deng, G., and Visonneau, M., "Cross wind effects on a simplified car model by a des approach," Computers & Fluids, Vol. 78, 2013, pp. 29–40.

Hoekstra, M., Eça, L., "Testing Uncertainty Estimation and Validation Procedures in the Flow Around a Backward Facing Step," Proceedings of the 3rd Workshop on CFD Uncertainty Analysis, Lisbon, Portugal, 2008.

Kornev, N., Taranov, A., Shchukin, E. and Kleinsorge, L., "Development of hybrid URANS-LES methods for flow simulations in the ship stern area," Ocean Engineering Vol. 38, Issue 16, pp. 1831–1838, 2011.

Larsson, L., Stern, F., and Visonneau, M., Numerical Ship Hydrodynamics, An assessment of the Gothenburg 2010 Workshop. Springer Verlag, 2013.

Leroyer, A., and Visonneau, M., "Numerical methods for RANSE simulations of a self-propelled fish-like body," J. Fluid & Structures, Vol. 20, No. 3, 2005, pp. 975–991.

Pržulj V. and Basara B., "Bounded convection schemes for unstructured grids," 15th AIAA Computational fluid dynamics conference, AIAA paper 2001-2593, 11-14 June, Anaheim, CA, 2001.

Queutey, P., and Visonneau, M., "An interface capturing method for free-surface hydrodynamic flows," Computers & Fluids, Vol. 36, November 2007, pp. 1481–1510.

Visonneau, M., Deng, G., Queutey, P., Wackers, J., and Mallol, B., "Anisotropic grid adaptation for rans simulation of a fast manoeuvring catamaran," 4th High Performance Yacht Design Conference, HPYD4, Auckland, New-Zealand, 2012.

Wackers, J., Deng, G., Guilmineau, E., Leroyer, A., Queutey, P., and Visonneau, M., "Combined refinement criteria for anisotropic grid refinement in free-surface flow simulation," Computers & Fluids, Vol. 92, 2014, pp. 209–222.